ADVANCED FUNCTIONAL MATERIALS
www.afm-journal.de

Intraocular Pressure Monitoring Smart Contact Lens with High Environmental Stability

*Huan Yang, Hengtian Zhu, Hanwen Liu, Zhengyi Mao, Junxian Luo, Shugeng Zhu, Zizhong Hu, Songtao Yuan, and Fei Xu**

Smart contact lenses (SCLs), integrating various functional components, serve as a platform for wirelessly intraocular pressure (IOP) monitoring. Accurate and dynamic measurements offer crucial clinical references for patients with ocular hypertension. Nevertheless, the complex ocular environment poses great challenges, particularly for inductor–capacitor–resistor (LCR) type IOP sensors, which suffer signal instability due to variations of ocular dielectric properties. Here, an innovative IOP monitoring sensor with robust environmental stability, achieved by integrating the ground shield, is proposed. Employing a capacitive pressure sensor with porous polydimethylsiloxane (PDMS) structure encased in a hydrogel, the study successfully demonstrates high-sensitivity monitoring of IOP changes using in vitro porcine eyes. This optimized design empowers the wireless IOP sensor with a sensitivity of 1.15 ‰/mmHg. It exhibits exceptional frequency stability after undergoing 100 wear cycles on ten distinct porcine eyes and remains reliable across a wide range of metabolite concentrations typical of normal eyes. Notably, any observed frequency shift translates into IOP changes within a 3 mmHg range, showcasing its suitability for repeated use and daily IOP monitoring.

1. Introduction

Glaucoma, often termed the "silent blinder" due to its gradual yet progressive visual impairment, is a severe ocular condition. It is frequently associated with elevated intraocular pressure (IOP), leading to optic nerve damage and, ultimately, potential blindness.[1] Meanwhile, symptoms of glaucoma are typically inconspicuous in the early stages, and patients may not be aware of their condition.[2] Therefore, it is imperative to monitor IOP and provide vital insights for personalized therapeutic interventions.[3] Goldmann applanation tonometry is the gold standard for measuring IOP,[4] primarily employed by trained hospital medical professionals. Nonetheless, studies have demonstrated that IOP follows a circadian pattern and exhibits significant fluctuations throughout the day and night.[5] Consequently, there is a necessity for a continuous IOP monitoring sensor that is free from the constraints of time and location.

Smart contact lenses (SCLs) leverage state-of-the-art technology to provide a range of advanced functionalities for monitoring crucial biomarkers,[6] including IOP, glucose, lactoferrin, and cholesterol.[7] Employing chip-free and battery-free designs, inductor-capacitor-resistor (LCR) based SCLs are being investigated as a solution for IOP monitoring.[7a,8] As IOP fluctuates, the cornea undergoes corresponding deformation.[9] This alteration is transmitted to the contact lens, influencing the capacitance or inductance of the LCR circuit and leading to a shift in circuit resonant frequency.[7a,8b,d] The circuit would also have a change in carrier mobility or shape, and the change in resistance or current is often used to reflect fluctuations in pressure.[7b,10] In IOP monitoring based on capacitive change, the observed frequency shift is an intuitive indicator of IOP changes, which is critical to achieving high sensitivity for precise measurements. Since capacitive sensors are affected by parasitic capacitance, the external environment in direct contact with the SCLs must be shielded to produce the same signal with the same pressure.

Of paramount importance, the eye constitutes a dynamic environment with tears undergoing constant renewal.[11] While numerous studies have focused on artificial models, in vitro porcine

H. Yang, H. Zhu, H. Liu, Z. Mao, S. Zhu, F. Xu
National Laboratory of Solid State Microstructures
College of Engineering and Applied Sciences, and Collaborative Innovation Center of Advanced Microstructures
Nanjing University
Nanjing 210023, China

J. Luo
School of Physics
Nanjing University
Nanjing 210008, China

Z. Hu, S. Yuan
Department of Ophthalmology
The First Affiliated Hospital with Nanjing Medical University
Nanjing 211166, China

F. Xu
Chemistry and Biomedicine Innovation Center (ChemBIC)
Nanjing University
Nanjing 210093, China
E-mail: feixu@nju.edu.cn

The ORCID identification number(s) for the author(s) of this article can be found under https://doi.org/10.1002/adfm.202400722

DOI: 10.1002/adfm.202400722

eyes, or static anesthetized rabbits, the influence of the eyelids on tear film composition, consequently affecting environmental permittivity and parasitic capacitance, is often overlooked.[12] In daily life, individuals may frequently wear and remove contact lenses, leading to alterations in the lens's dielectric environment. This introduces a frequency shift unrelated to pressure changes, posing a challenge to distinguish it from pressure-induced shifts and leading to significant discrepancies in IOP measurements. Chen et al.'s previous research indicated that tear composition variations could introduce an IOP measurement error of up to 10 mmHg.[13] Karunaratne et al.[12] proposed a dual-resonator sensor to mitigate environmental effects. Lee et al.[14] suggested a hybrid mechanical design strategy incorporating dual compliance and a dual-contact lens sensor to minimize noise. Nevertheless, their structural designs are notably intricate, and the placement of two coils may obstruct the line of sight. In the case of LCR sensors for skin, Amirhossein employs a shielding layer similar to that of the coil to minimize interference due to variations in fit to the skin.[15]

Here, we introduced a SCL with robust capabilities to mitigate environmental effects and specifically designed for precise IOP monitoring. To surmount the above challenges, we employed a polydimethylsiloxane (PDMS) written with microbubbles, inscribed using a femtosecond laser, within the sensor's dielectric elastomer. It was a strategy optimized for maximizing capacitance change under uniform pressure due to its low effective elastic modulus.[16] Validation of the sensor's performance included pressure response assessments conducted in a vitro porcine eye, yielding a sensitivity of 1.15 ‰/mmHg (one thousandth per mmHg). Most importantly, employing dual copper foil ground layers, we effectively shielded against external influences, ensuring sustained frequency stability in our SCLs. We examined resistance to fluctuations in the concentration of multiple tear metabolites on the prosthetic eye model, resulting in a 2 mmHg conversion of frequency shift to IOP change. Our SCLs exhibited unwavering stability after 100 wear cycles across ten distinct vitro porcine eyes. Any frequency shift observed translated into IOP changes within a 3 mmHg range. We performed pressure response tests on ten different porcine eyes with a fitted sensitivity of 1.20‰/mmHg. To underscore the transformative potential of our sensor in practical settings, we extended our assessments to living rabbits, reaffirming their capability to resist environmental influences. The frequency stability was one order of magnitude higher than that of ordinary coils. These designs ensured that SCLs could be used in complex and dynamic environments and with diverse populations.

2. Experimental Section

2.1. Design and Fabrication of Environmentally Stable IOP Sensor

Figure 1a demonstrates the corneal deformation in response to the IOP variation, serving as the foundational inspiration for the innovative IOP monitoring contact lens. This device consisted of four distinct layers: an inductive coil, two shielding layers, and a dielectric layer featuring bubble-filled PDMS, all of which were carefully assembled. The micrograph of each layer is depicted in the inset of Figure 1a. A pHEMA hydrogel was employed to encapsulate these layers to ensure seamless attachment on the cornea, creating a smooth surface that harmoniously conformed to the eye's contours. The bubbles in the PDMS were prepared using a femtosecond laser, a process that proved to be straightforward. Details of the sensor's preparation are provided in the Experimental Methods section and are visually elaborated in Figure S1 (Supporting Information). The study used a mold that allowed the light from the UV lamp to pass through the mold for photoinitiated curing, as shown in Figure S2a (Supporting Information). The dimensions of the mold are shown in Figure S2b (Supporting Information), which had a base arc of 7.8 mm and an outer diameter of 13.8 mm and was comparable to the size of a commercial contact lens. The SCLs, as depicted in Figure 1b, had impressive light transmittance, and the functional structures were strategically positioned at the edge of the contact lens. The encapsulated SCL was cut in the middle, as shown in Figure S2c (Supporting Information), and it fitted closely to the commercial contact lens mold, which indicated that the SCL size was similar to the commercial one. The study measured the thickness of the center of the SCL, and the microscope image is shown in Figure S2d (Supporting Information), with a thickness of 180 µm. The study further measured the thickness of the sensing region. As shown in Figure S2e (Supporting Information), the thickness of the area is 540 µm due to the inclusion of the functional devices. These results show that the SCL ensured an unobstructed line of sight and maintained base arc and diameter dimensions identical to standard commercial contact lenses, guaranteeing the wearer a comfortable and secure fit.

The resonant frequency f_s of the sensor can be expressed as:

$$f_s = \frac{1}{2\pi\sqrt{L_s C_s}} \tag{1}$$

where L_s and C_s are the sensor's inductance and capacitance separately. Parallel plate capacitive sensors are characterized by a dielectric between the electrodes and produce changes depending on the distance between the two electrodes. It can be expressed by a simple equation:

$$C_s = \frac{\epsilon_r \epsilon_0 A}{d} \tag{2}$$

where ϵ_r, ϵ_0, d, and A represent the vacuum permittivity, dielectric constant, and gap between the top and bottom electrodes and the overlapped electrode area, respectively. Information on the coil can be extracted through a reading coil externally connected to the vector network analyzer (VNA), with the state of the SCL represented by the reflection coefficient (S_{11}) curve. Equation (1) reveals that augmenting the capacitive response leads to an increase in frequency response, enhancing the sensitivity of IOP monitoring. A bubble-filled PDMS with a lower modulus was sandwiched between the coil and shielding layer. As illustrated in Figure 1c, the dielectric elastomer PDMS within the sensor exhibited enhanced deformation compared to non-bubble-filled PDMS at identical pressures. This amplification translated to a greater change in capacitance and, consequently, a heightened frequency shift, yielding heightened sensitivity. The femtosecond laser processing gave the PDMS a three-layer bubble structure. As shown in Figure S3a (Supporting Information), the bubbles are written in the PDMS, and it was observed with a

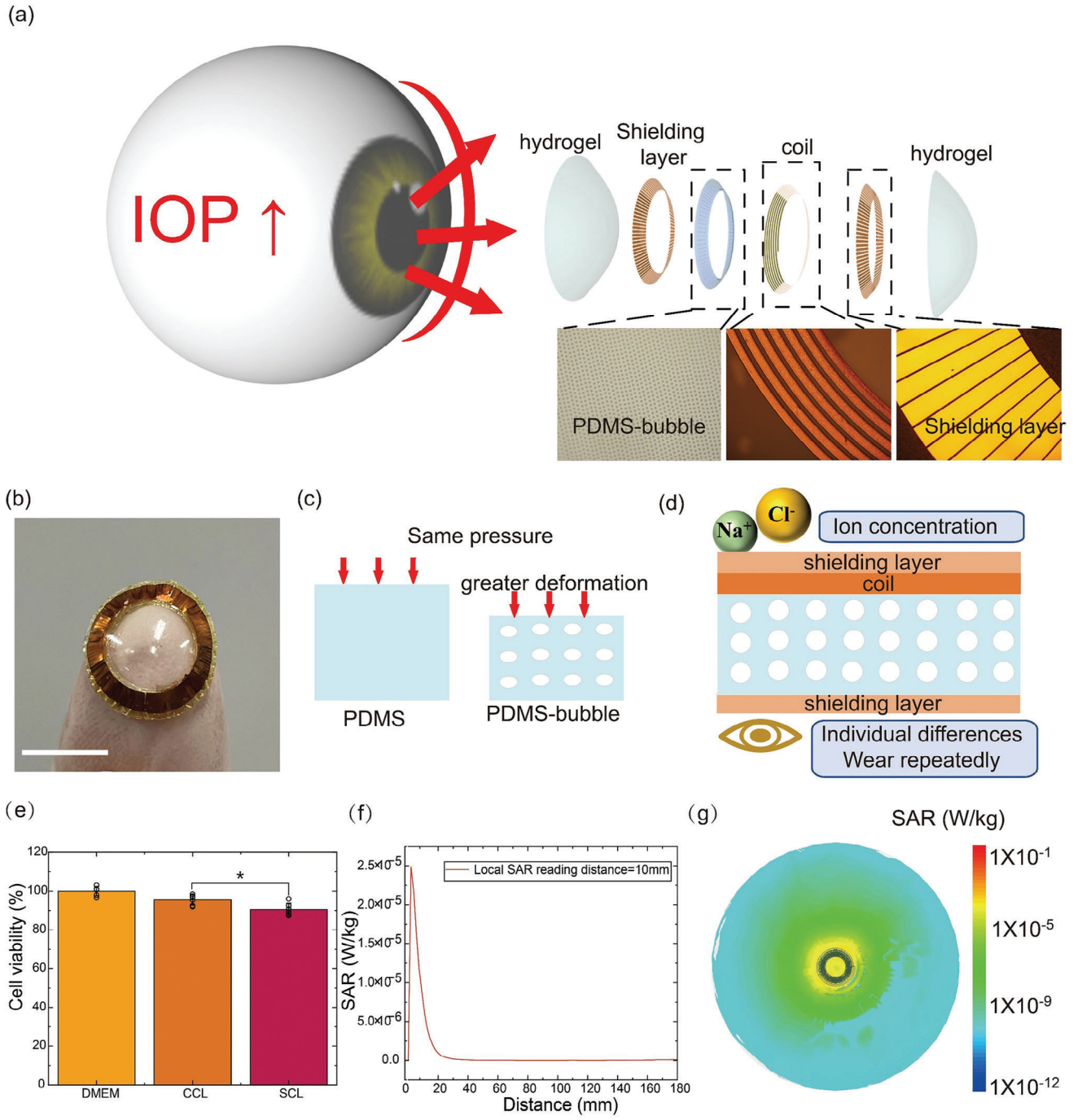

Figure 1. Design and principle of environmentally stable SCL for IOP monitoring. a) Schematic diagram of the human eye under IOP changes and hierarchical structure diagram of the IOP monitoring SCL. b) Photograph of the SCL. Scale bar 1 cm. c) Comparison of deformation of different structures of PDMS as capacitive dielectric elastomers at the same IOPs. d) Schematic diagram of a sensor containing two additional layers of shielding and the shielded factors. e) 24-hour cytotoxicity test of SCL using human corneal cell lines ($n = 6$). f) SAR simulation results on a human head as a function of the distance between the head and the SCL. g) SAR simulation results in a human head.

microscope in the X-Y direction and cut it in the Y-Z direction to look at bubbles. As shown in Figure S3b (Supporting Information), the bubbles are written in parallel in PDMS. Figure S3c (Supporting Information) shows that the bubbles are written at different depths in the PDMS. Figure 1d provides a schematic representation of the sensor incorporating two additional shielding layers. The presence of two shielding layers ensured that the sensor was not subject to additional parasitic capacitance due to changes in the dielectric environment of the eye caused by metabolites concentration, individual

differences, and repeated wear. This design feature ensured the robust and stable operation of the SCLs under the intricate and dynamic conditions of the eye. To verify the cytotoxicity of the SCL, the viability of cells from human corneas (HCE-T) was measured. Extracts of the SCL were prepared by immersing the lenses into the cell culture medium for 24 h. After culturing the cells using extracts for 24 h and then adding CCK-8 reagent, the absorbance was measured to record the viability of the cells. More details are provided in the Experimental Section. As shown in Figure 1e, the cell viability using extracts of the SCL remained above 90% after 24 h of incubating, with no notable differences among the groups. This suggests that the SCL was non-cytotoxic over daily wear and would pose little risk of corneal inflammation. Electromagnetic effects from SCLs need to be considered when the human eye is exposed to electromagnetic environments. Finite element analysis was conducted to simulate the maximum Specific Absorption Rate (SAR) for a person's head.[17] Figure 1f,g shows the result, which indicates that the maximum SAR value of this SCL was only 2.5×10^{-5} W kg^{-1}. This value was well below the regulation value (2 W kg^{-1}).[18] This suggests that this SCL will not cause electromagnetic damage to the eyes when exposed to electromagnetic environments.

2.2. Design and Optimization of Bubble-Filled PDMS and Shielding Layer Structures

A bubble-filled dielectric elastomer was strategically employed between the capacitive sensor's coil and the shielding to heighten sensitivity in detecting IOP. PDMS was selected as the dielectric material and processed with a femtosecond laser, and the number of layers of the bubble could be controlled, as shown in **Figure** 2a. To assess the performance of PDMS with varying numbers of bubble layers, the study conducted finite element simulations on structures with different bubble configurations. Figure 2b illustrates the deformation of PDMS with three layers of bubbles. Structures were simulated with 0, 1, 2, and 3 layers, revealing that the three-layer configuration exhibited the most considerable deformation under the same pressure, with a 60% improvement compared to the sample devoid of bubbles. The red star in Figure 2c represents the three-layer bubble sample, which ultimately became the adopted bubble structure. Details of the other layers are shown in Figure S4 (Supporting Information). The more layers there are, the greater the deformation at the same pressure. The three-layer bubble in this work is a trade-off between effectiveness, efficiency, and sensitivity. The study also explored bubble size, as shown in Figure S5 (Supporting Information), where the larger the bubble, the more significant the relative change in capacitance for the same number of layers. The performance improvement was mainly due to the introduction of bubbles. As the bubbles begin to collapse upon applied pressure, the ratio of air to elastomer decreases, leading to an increase in the effective dielectric constant since the elastomer typically had a higher dielectric constant than air.[19] The study also conducted the distribution of the bubbles. Figure S6 (Supporting Information) indicates that the distribution of bubbles in the PDMS does not affect the pressure response under the same bubble size and the same number of layers.

For practical validation, samples with different bubble layers were fabricated and characterized by planar pressure, and the schematic diagram of the test setup is detailed in Figure S7 (Supporting Information). A computer-controlled push-pull force meter gradually applied pressure to a flat sample positioned on a quartz glass plate while the VNA recorded the S_{11} curve. The sample used PDMS containing three layers of bubbles as the elastic dielectric. The resulting pressure response S_{11} curves are depicted in Figure 2d. The planar pressure sensitivity was computed, as shown in Figure 2e, and assessed the lower-sensitivity region for comparison. The outcomes of the planar characterization for other layer structures are presented in Figure S8 (Supporting Information). Figure 2f provides a comparison of the sensitivity results, revealing that the three-layer bubble sample demonstrated a sensitivity twice as high as the blank sample. These findings underscored that incorporating bubbles within the PDMS effectively enhanced the device's sensitivity.[20]

Numerous studies have explored LCR pressure sensors utilizing variations in the dielectric environment.[21] However, minimizing the influence of the dielectric environment is imperative to ensure the precision of IOP measurements. The shielding layers served to counteract interference arising from alterations in environmental dielectric property. As shown in Figure S9 (Supporting Information), when adding a shield on one side of the coil, the electric field on the side was confined between the shield and the coil. The shield blocked out the parasitic capacitance generated by the coupling between the coil and the external environment. The shielding layer terminated eddy currents by setting up gaps and maintaining the resonator's quality factor.[15,22] As illustrated in Figure 2g, segmenting the shield into slot widths and gaps, with one width and one gap constituting a period, allowing for improved resistance to interference. For simplification in finite element simulations, the study evaluated performance by comparing the frequency shift of the SCL when in contact with the cornea and when positioned away from it (1 cm). Maintaining a consistent period, the duty cycle was adjusted and observed that higher duty cycles caused more minor frequency shifts, as demonstrated in Figure 2h. Conditions were reversed and noted that, with a consistent duty cycle, shorter periods resulted in diminished frequency shift, depicted in Figure 2i.

Simulation outcomes identified a structural configuration featuring a slot width of 2.8° and a slot interval of 0.2° as optimal. This configuration exhibited a frequency response deviation of 2.2‰ when in contact with and away from the cornea while concurrently achieving the highest quality factor. Consequently, this structural design for sample preparation was adopted, as illustrated in Figure 2j. To show the performance of the structure, the study gradually approached the sample with the shielding layer and the unshielded coil to the vitro porcine eye and measured the resonance frequency in this process. As shown in Figure 2k, the shielding sample maintained resonant frequency stability from air to gradually contacting porcine eyes. Conversely, Figure 2l illustrates a significant shift in resonance frequency for the unshielded coil as it approached the vitro porcine eye. These results indicated that the blank coil was strongly disturbed by changes in the surrounding dielectric environment, which the shielding layer could effectively attenuate. This

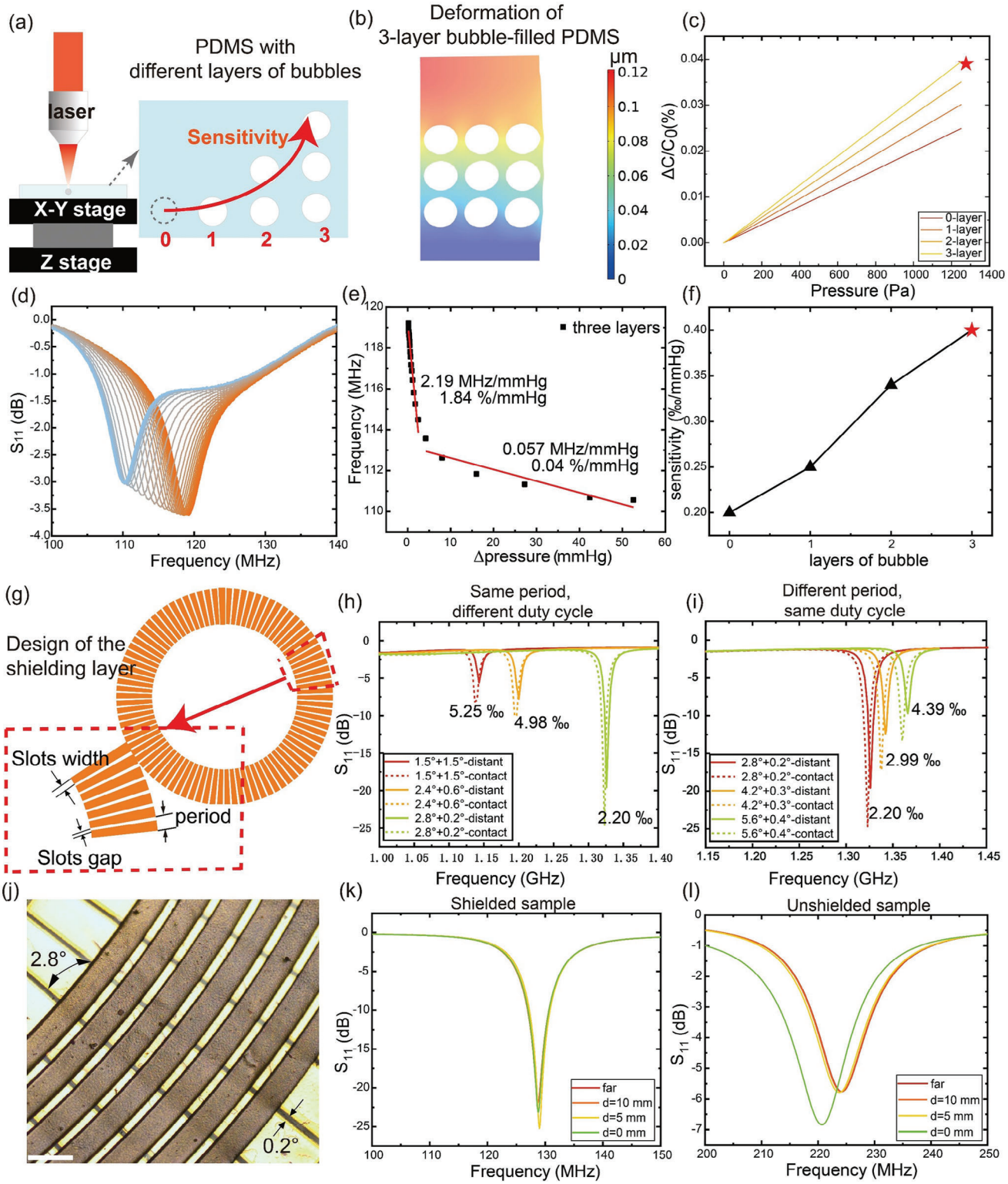

Figure 2. Structural optimization of bubble-filled PDMS and shield layers. a) Femtosecond processing and sensitivity enhancement of PDMS with different layers of bubbles. b) Simulation of deformation under pressure of PDMS filled with three layers of bubbles. c) Simulation comparison of the relative change in capacitance under pressure for PDMS with different number of layers of bubbles. d) S_{11} curves of planar pressure characteristics of three-layer bubble PDMS. e) The pressure response of a three-layer bubble PDMS. f) Comparison of pressure sensitivity of PDMS with different number of bubble layers. g) Shielding layer structure. h) Performance simulation of shielding structures with the same period and different duty cycles. i) Performance simulation of shielding structures with different periods and the same duty cycle. j) Microscopic view of coil and shield assembly. k) Frequency response of shielded SCL close to vitro porcine eyes. l) Frequency response of unshielded SCL close to vitro porcine eyes.

pivotal development established a robust foundation for precise IOP monitoring.

After determining the structure of the dielectric elastomer and the shielding layer, the repetitive stress tests of 2000 cycles under a pressure of 0.6 N were carried out using the flat samples. The repeatability and stability of SCLs are shown in Figure S10 (Supporting Information). The inset shows the details of 100 of these cycles. These results demonstrated that the SCL exhibited minimal deviation in device performance after undergoing 2000 repetitive cycles, attesting to its commendable repeatability and robustness.

2.3. Preparation of the PDMS

A 10 wt% aqueous solution of polyvinyl alcohol (PVA) (Macklin P816865) was first spin-coated on a clean slide at 600 rpm for 30 s and then heated on a heater at 100 °C for 10 min. The PDMS solution consisted of a 10:1 ratio of base and curing agent and was stirred three times in a vacuum rotator and stripped of air bubbles. It was then spin-coated onto PVA-coated slides at 1000 rpm for 30 s and then cured on a heater at 80 °C for 2 h. A femtosecond laser was then used to write bubbles inside the PDMS. The slide was immersed in water for 12 h to dissolve the PVA in the water, and the PDMS was automatically peeled off the slide. PDMS was punched into a circular shape as a dielectric elastomer using 8 and 13 mm diameter punches, respectively.

2.4. Femtosecond Processing of Micro-Bubble Structure in PDMS Film

A commercial femtosecond laser (Pharos PH2-20 W, Light Conversion) was used in this experiment. Several technical characteristics of this laser were as follows: 20 W maximum average power, 400 μJ maximum single pulse energy, 290 fs pulse width, and 1 MHz maximum repetition rate. To further control the laser energy, a motorized ultrafast variable attenuator (VA-BB CONEX, MKS Newport) was used, in which a half waveplate could be rotated to dynamically tune the extinction ratio dynamically. In this experiment, single pulse energy was set to 8.9 μJ, and the repetition rate was set to 7143 Hz. In addition, the laser was operated in the burst mode (P = 3, N = 3) to minimize thermal damage to the PDMS. In burst mode, a single femtosecond pulse was divided into a pulse train containing several sub-pulses. In the case of P = 3, and N = 3, the pulse train contained nine sub-pulses. The study used two motorized stages (V551.4d and V551.2d, Physik Instrumente GmbH) to move the sample in X and Y directions respectively, and the Z position of the objective (Nikon LU Plan ELWD 100x, NA = 0.8) was controlled by a manual stage to achieve 3D manufacturing capability. The bubble array was formed in PDMS film by raster scanning the sample with a maximum speed of 85 mm s^{-1}, and the spacing between each row was 12 μm. Each bubble was created by the micro explosion induced by one single shot of the tightly focused femtosecond pulse. Microscope and SEM images of the bubble can be found in Figure S3 (Supporting Information).

2.5. Fabrication Process of Smart Contact Lens

The fabrication of the SCLs involved the preparation of the shielding layer and coils, stacking and assembly of each layer of devices, and hydrogel encapsulation. As shown in Figure S1 (Supporting Information), spin-coating 1.5 μm thick polyimide (PI) on a clean piece of glass substrate and then the copper seed layer with a thickness of 200 nm was e-beam deposit. The copper was patterned using the standard photolithography process, and the patterned areas were directionally thickened by electroplating. The final copper thickness was 5 μm to ensure the quality factor of the resonant signal. After removing the photoresist and wet etching the seed layer, another layer of PI was spin-coated on top of the pattern for insulation. Then, patterned cutting of PI with laser (450 nm, 1600 mW, Snapmaker). The flexible coils and shielding layers were lifted off the glass after being immersed in the water, reducing the attachment between the PI and the glass. Subsequently, two shielding layers, a coil, and a three-layer bubble of PDMS were stacked together, encapsulated with a homemade contact lens mold with hydrogel, and irradiated with 365 nm, 10 mW power UV light for 20 min. After the contact lens was removed from the mold, it was in distilled water to replace the solvent.

2.6. Synthesis of pHEMA Hydrogel

2-hydroxyethyl methacrylate (HEMA, Energy Chemical) as the monomer, 10 wt% polyethylene glycol dimethacrylate (PEGDMA600, Macklin), 0.2 wt% bis(2,4,6-trimethylbenzoyl)phenylphosphine oxide (Macklin) as photoinitiator, 38 wt% glycerol (Aladdin) as a solvent, and 25 wt% tertiary butyl alcohol (Xilong Scientific) were mixed for more than 3 h at room temperature.

Pour 80 μL of the monomer mixture into a homemade contact lens mold and irradiate it with UV light at 365 nm with a power of 10 mW for 20 min. After polymerization and demolding, the SCL was soaked in deionized water to replace the solvent.

2.7. Plane Pressure Response Test

Stress was applied and calibrated by a push-pull gauge (HANDPI SH-2N). A near-field reader (Shezhen Huanqiu Xinrui Electronic Technology Co., Ltd) connected to a VNA (Agilent e5072a ENA) was placed under the smart contact lens to detect its resonant frequency wirelessly.

2.8. Prosthetic Eye IOP Test

The prosthetic cornea was made of PDMS with a 10:1 ratio of base and curing agent, with a thickness of 200 μm, a base arc of 8.6 mm, and an outer diameter of 13.8 mm. IOP was controlled by an injection syringe connected to the prosthetic eye model and calibrated by a static pressure meter connected to a tee tube. The frequency response was read by a near-field reading coil placed over the smart contact lens connected to a VNA (Agilent e5072a ENA).

2.9. Porcine Eyes IOP Experiment

In vitro experiments were performed using porcine eyeballs. The IOP of the eyeball was controlled by a syringe pump, with a needle inserted into the aqueous humor area of the eyeball and calibrated by a hydrostatic pressure gauge via a liquid tee. Changes in resonant frequency were characterized wirelessly using a network analyzer (Agilent e5072a ENA) with a near-field reader fixed vertically above the SCL.

2.10. Configuration of Different Tear Metabolites

Sodium chloride (Solarbio Life Sciences), glucose (Xilong Scientific), ascorbic acid (Aladdin), and protein (lysozyme, Macklin) were selected as metabolites for resonance frequency stability testing. Their concentrations are shown in Table S1 (Supporting Information). All solutions were configured by mixing with deionized water according to the concentration ranges.

2.11. In Vivo Performance in Rabbit

All animal experiments were performed according to the National Institute of Health Guidelines under the protocols approved by the ethics committee at the Nanjing Medical University (SYXK(Su)2021-0023). Female New Zealand White rabbits (3 kg) were used for the test to determine the stability of the devices after repeated wear and changes in ion concentration. The rabbits were immobilized during the experiment using a homemade fixator and kept in an open eyelid position using an eye support. SCLs with and without the shielding layer were worn ten times in the right eye of the same rabbit. In the test of the stability of SCLs by changes in chloride ion concentration, rabbit eyes were rinsed with 118, 128, and 138 mM sodium chloride solutions, and then the S_{11} curves were collected.

2.12. Cytotoxicity Tests

Human corneal epithelial cell lines (HCE-T) were employed to test cytotoxicity. HCE-Ts were maintained in DMEM/F-12, supplemented with 10% fetal bovine serum (FBS), and 1% penicillin-streptomycin (P/S, Gibco) (complete medium) at 37 °C in a humidified atmosphere of 5% CO_2 with medium change every 3 days. After several passages, these cells were harvested and plated at a density of 5000 cells per well. The cells were incubated in a complete medium for 24 h.

Before the experiment, samples were immersed in deionized water, and the water was changed four times a day for three consecutive days to remove solvents such as tert-butanol and glycerol. Then, the samples were sterilized with ultraviolet irradiation for 12 h. In addition, a complete medium (DMEM) was used as a control group, and extracts of bare commercial contact lens (CCL) were used as the comparisons. Extracts were prepared by immersing the different samples into the cell culture medium at 37 °C for 24 h. The extracts were prepared with samples of 0.2 g in the complete medium of 1 ml according to ISO 10993–5. After several passages, the medium of cells was changed to different extracts for the cell viability test (n = 6) within 24 hours using a cell counting kit-8 assay. The absorbance was read at 450 nm using a multimode plate reader. The absorbance values were converted into percentage values relative to the absorbance obtained from cell growth media alone.

2.13. Specific Absorption Rate (SAR) Simulation

Finite element analysis was conducted to simulate the maximum SAR for a person's head. The simulations were performed using Ansoft HFSS. In the simulation, the SCL's antenna and the shielding layer were located under the human head model (radius 9 cm), and the transmitting power from the reading coil was set as 0 dBm (1 mW) for the electromagnetic exposure safety test. The distance between the SCL and the reading coil was 10 mm.

3. Results and Discussion

3.1. Characteristics of Smart Contact Lens

The three-layer bubble sample maintained high sensitivity after being encapsulated in the hydrogel. **Figure 3a** illustrates using a PDMS-based prosthetic eye model platform for testing the SCLs, where the lens was positioned atop the model. A syringe was inserted into the prosthetic eye model, and the IOP was controlled by injecting air, and the real-time pressure was displayed by the pressure gauge. During the pressure test, we used pure water to moisten the surface of the eye until making sure there was a layer of water on both sides of the SCL and completed the test as quickly as possible to minimize the effects of water loss from the hydrogel. The deformation of the prosthetic eye model under different IOPs was successfully detected by SCLs, as shown in Figure 3b. As depicted in Figure 3c, the sensitivity on the prosthetic eye model stands at 1.00 ‰/mmHg, covering the typical IOP range of individuals with glaucoma.[2]

To closely mimic the physiological environment of the human eye, we used an in vitro porcine eye instead, as its curvature is close to that of the human eye. As shown in Figure 3d, the surface of the porcine eye contained pure water, simulating the natural tear environment as much as possible. The IOP was controlled in the same way as the prosthetic eye model. The SCLs were fitted onto the surface of the porcine eyes without obstructing vision. Figure 3e shows the S_{11} curves at different IOPs. Due to the hydrophilic nature of the hydrogel-encapsulated SCLs, they adhered more closely to the vitro porcine eye, resulting in a heightened sensitivity compared to the prosthetic eye model. As shown in Figure 3f, a sensitivity of up to 1.15 ‰/mmHg was achieved within the range of 40 mmHg. Repeatability tests were conducted on the prosthetic eye model and the porcine eye, indicating satisfactory stability, as presented in Figure S11 (Supporting Information).

3.2. Characterisation of the Environmental Stability of Smart Contact Lens

A prior investigation has demonstrated that tonometry exhibits variations between individuals at identical IOP levels.[23] Moreover, within the same individual, the various physiological markers in tear fluid undergo continuous renewal due to metabolic

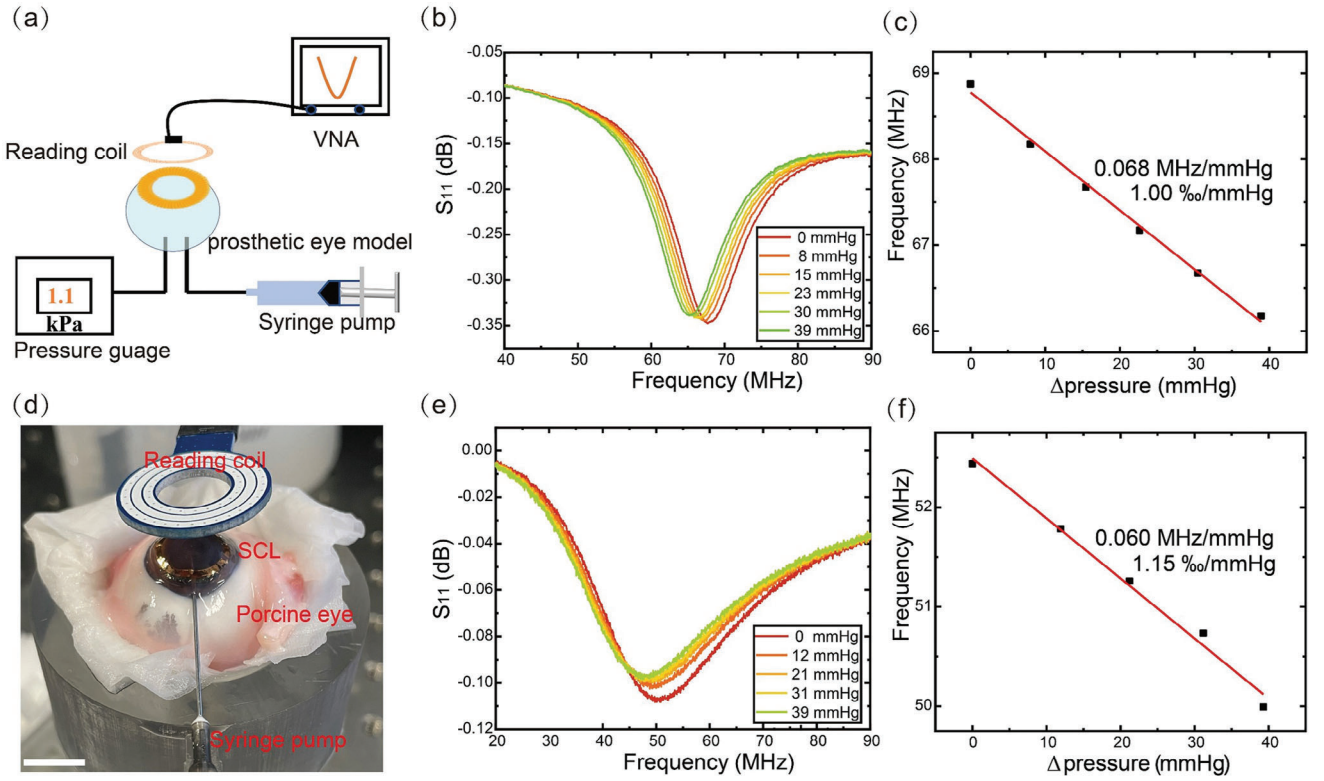

Figure 3. Schematic diagram of pressure characterization of smart contact lenses. a) Schematic diagram of experiment setup for IOP monitoring on a prosthetic eye model. b) Return loss response with different pressures on the prosthetic eye model. c) Pressure response sensitivity on the prosthetic eye model. d) Photograph of monitoring IOP using in vitro porcine eyes. Scale bar 1 cm. e) Return loss response at each pressure on the porcine eye. f) Pressure response sensitivity on the porcine eye.

processes. Additionally, the composition and structure of the tear film evolve with each blink, rendering the ocular environment a highly intricate and dynamic milieu. Individual differences in corneal structure, fluctuations in ionic concentration, and alterations in the eye's environment during repeated wear further contribute to the variability in dielectric environments experienced by SCLs. As shown in **Figure** 4a, the parasitic capacitance affected by the surrounding environment becomes uncertain, leading to a substantial frequency shift for typical LCR sensors. This deviation potentially imparts significant misinformation on IOP monitoring, considering the sensitivity of the LCR sensor. In order to explore the interference of ion concentration, the sodium chloride (NaCl) solutions of different concentrations were added to the SCLs on the prosthetic eye model. Concerning the chloride concentration of normal human eyes, NaCl solutions with a concentration of 98–168 mM were selected in our experiments. To compare the resonant frequency distributions more intuitively, we normalized the S_{11} curves. As evidenced by the S_{11} curves in Figure 4b, the resonant frequency of SCLs with shielding layers exhibited convergence. Although there was a frequency change in the SCLs with a shield when comparing them to those in pure water, the frequency remained relatively stable over the range of NaCl concentrations in the tear fluid. In contrast, samples lacking the shielding layer observed a marked resonant frequency shift. We converted the percentage change in frequency from 98 to 168 mM into IOP using the pressure response sensitivity of the prosthetic eye, which was 2 and 75 mmHg, respectively. In addition to NaCl, there are many metabolites in the tear fluid, as shown in Table S1 (Supporting Information). We selected glucose, ascorbic acid, and protein for testing. The results in Figure S12 (Supporting Information) show that SCLs with a shield were much more stable than those without a shield. The outcomes affirmed that SCLs lacking this shielding layer may yield significantly erroneous information to users. In Figure 4c, shielded and unshielded samples were worn ten times on ten distinct porcine eyes, amounting to 100 trials, and the S_{11} curve was recorded on each occasion. The frequency response curves of the two samples, as depicted in Figure 4d, reveal that the resonance frequency of the shielded sample exhibited greater concentration, while the frequency variation of the unshielded sample spanned nearly 10 MHz. To facilitate a more discerning comparison, we present the resonant frequency in Figure 4e. It can be seen that the degree of dispersion without shielding was higher. The variances shielded and unshielded were 0.161 and 1.17 MHz, respectively, which meant that SCLs with shielding were more stable over repeated wear. Employing a sensitivity of 1.15 ‰/mmHg, we calculated the variance translated into IOP fluctuations, which were 3.0 and 9.6 mmHg, respectively. The resonant frequency distributions were examined for each of the ten vitro porcine eyes, and the variance results in Figure 4f conclusively demonstrate that SCLs equipped with shielding effectively surmount the individual disparities among the eyes. Furthermore, as depicted in Figure 4g, the frequency distribution exhibits a higher degree of concentration, signifying

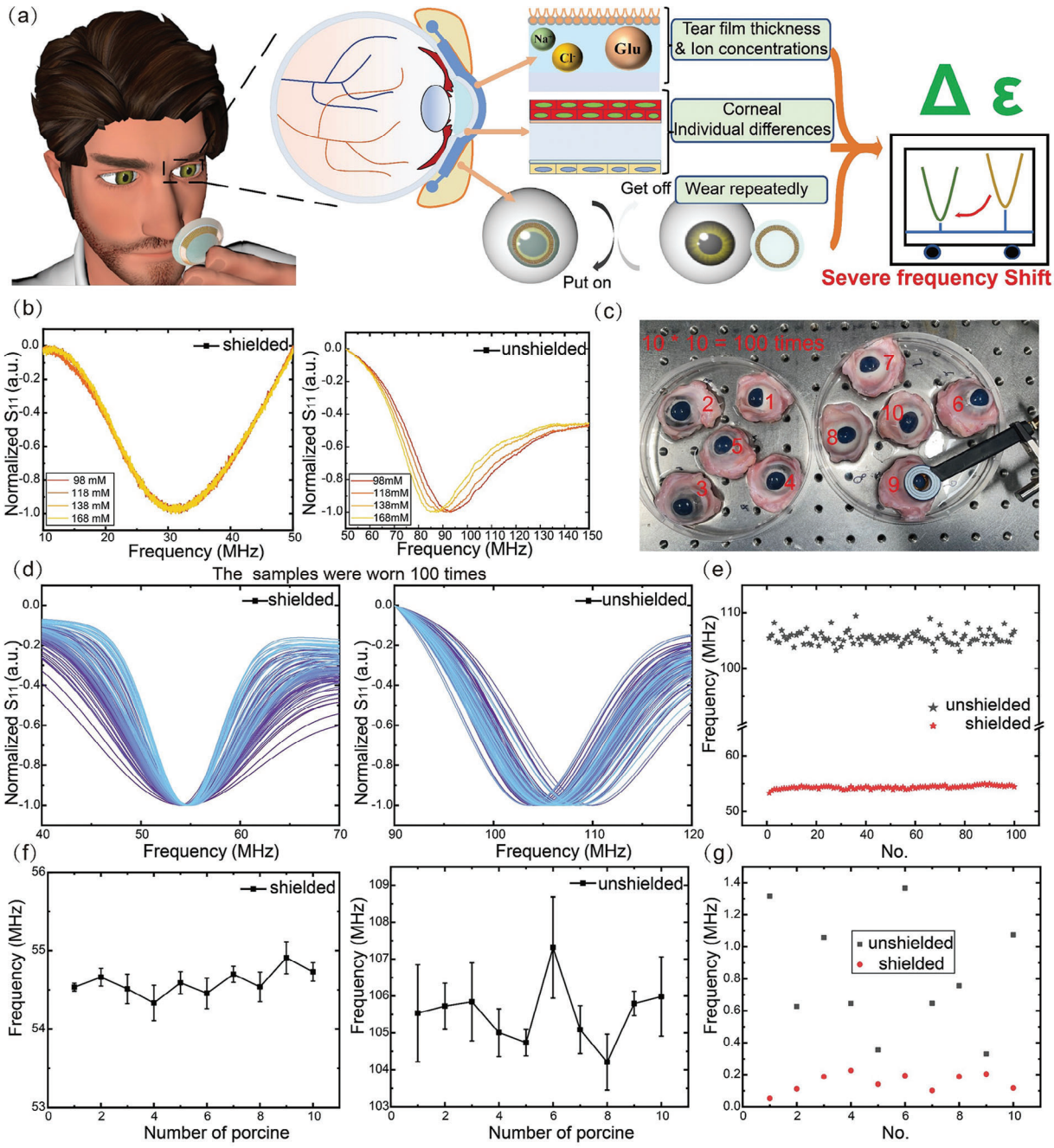

Figure 4. Characterization of resistance to interference from multiple dielectric variations. a) Diagram of daily wearing SCLs and factors that could change the eye's dielectric environment. The figure was adapted under the Creative Commons Attribution 4.0 International License. [24] Copyright 2024, Canino3d, Sketchfab, Inc. b) S_{11} curves of shielded and unshielded smart contact lenses worn on a prosthetic eye model under different chloride ion concentrations. c) Stability and resistance to individual differences were tested on ten porcine eyes. d) S_{11} curves of shielded and unshielded SCLs worn on ten different pig eyes. e) Distribution of a total of 100 resonance frequencies of the two samples. f) Variance statistics of the resonance frequencies of the two samples at each of the ten porcine eyes. g) Comparison of the variance distribution of frequencies on the eyes of ten pigs concerning resistance to individual differences.

that SCLs can be reliably employed across diverse populations. In direct comparison with prior studies,[12,14] we have achieved a comparable level of resistance against environmental dielectric interference. To verify the reproducibility of their sensitivity, SCL successfully collected pressure response data on ten different porcine eyes. The images during the test are shown in Figure S13a (Supporting Information). This SCL successfully collected pressure response data on ten different porcine eyes, and their S_{11} plots are shown in Figure S13b (Supporting Information). As shown in Figure S13c (Supporting Information), we counted the

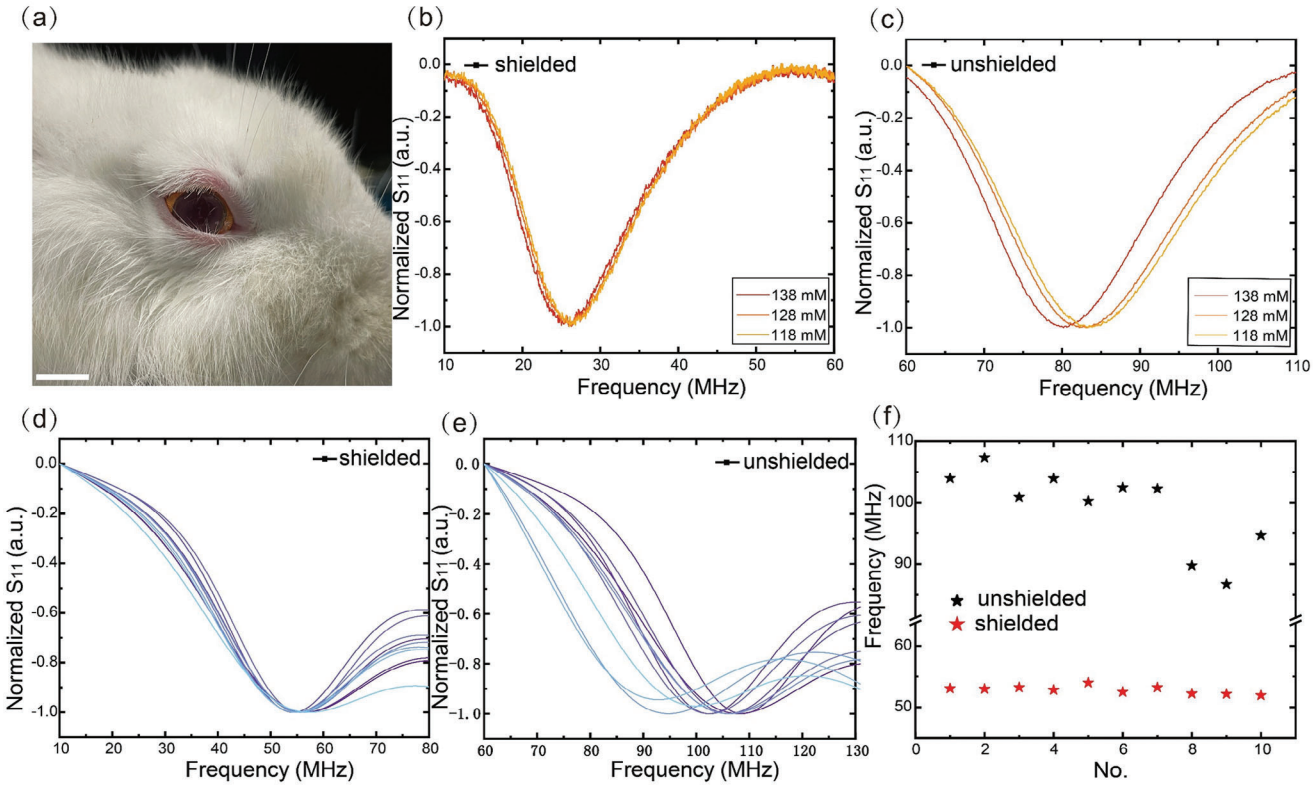

Figure 5. Characterization of the environmental stability of SCLs in the rabbit eye. a) Photograph of a rabbit wearing the SCL. Scale bar 1 cm. S_{11} curves of b) shielded and c) unshielded SCLs worn on a rabbit eye with different chloride ion concentrations. d) S_{11} curves of shielded SCLs worn on rabbit eye. e) S_{11} curves of shielded SCLs worn on rabbit eye. f) Statistical comparison of the resonant frequencies of shielded and unshielded SCLs.

sensitivity of these ten porcine eyes and performed a linear analysis, with a sensitivity of 1.20 ‰/mmHg, with a strong correlation ($R^2 = 0.89$). The results demonstrate the potential of SCLs for IOP detection in different individuals.

3.3. In Vivo Resistance to Ocular Dielectric Environmental Interference Testing

Live rabbits were employed for stability assessments amidst variations in ion concentration and repeated wearing to test the ability to resist ocular dielectric environmental interference in an environment closer to the human eye. As depicted in **Figure 5a**, the rabbit's eye wore a SCL that exhibited an optimal fit with the cornea, allowing for unobstructed vision and natural eyelid movement. A picture of the wearing details is shown in Figure S14a (Supporting Information). To facilitate data measurement, we fixed the rabbit and read the data with an outside reading coil, as shown in Figure S14b (Supporting Information). When testing for interference in ion concentration, we employed saline solutions ranging from 118 to 138 mM to rinse the rabbit's eyes, followed by a subsequent collection of the S_{11} curve. Analogous to the prosthetic eye model, the resonant frequency of the SCL equipped with a shielding layer, as illustrated in Figure 5b, exhibited a higher degree of concentration. In contrast, the sample lacking a shielding layer, as shown in Figure 5c, demonstrated a substantial frequency shift. The SCL's resonant frequency variances were 0.16 and 4.3 MHz for those with and without the shield, respectively. We conducted ten repetitions of wearing the SCLs, both with and without a shielding layer, on the same eye of the rabbit and recorded the S_{11} curve. As depicted in Figure 5d, the frequency of the SCL with the shield remained stable over ten cycles, whereas in Figure 5e, the frequency distribution without the shield spanned a broader range. The resonant frequencies are compared in Figure 5f, with variances recorded at 0.62 and 6.7 MHz, respectively. The tests on live rabbits unequivocally demonstrate that SCLs equipped with a shielding layer can effectively reduce interference from alterations in the eye's dielectric environment by an order of magnitude. This signifies a significant reduction in environmental disturbances when conducting real-time IOP monitoring, offering a pragmatic solution for continuous and precise IOP monitoring.

4. Discussion

In conclusion, we have demonstrated an SCL designed to resist external environmental interference, facilitating real-time wireless monitoring of IOP. The hydrogel encapsulation ensured a tailored fit to the cornea, meeting the unique environmental demands of the eye. We achieved heightened sensitivity using PDMS with three layers of microbubbles as the dielectric elastomer. We have effectively demonstrated IOP monitoring in vitro porcine eyes, attaining an impressive sensitivity of 1.15 ‰/mmHg. In addition, two shielding layers were used to

resist interference caused by dielectric changes in the environment. In in vitro testing, the stability of repeated wear produced an error margin of a mere 3 mmHg, and the influence of ion concentration registered an error margin of 2 mmHg. Even in live rabbits, our SCLs exhibited stability, surpassing conventional counterparts by an order of magnitude. With these exceptional performance characteristics and a refined design, our wireless, environmentally stable IOP monitoring SCLs hold significant potential to advance as next-generation devices for daily health management.

The Q-factor of the SCL is somewhat attenuated due to the introduction of the shield, while a high Q-factor is important for an accurate reading of the resonant frequency during IOP measurements. To achieve high Q-factor IOP detection, PT symmetry or impedance matching circuits can be used in future work to enhance the reading distance and reading accuracy of the device.[7a,25] There is also a need for more compact and miniaturized sensitization strategies to optimize the size of SCLs for future clinical applications.

Supporting Information

Supporting Information is available from the Wiley Online Library or from the author.

Acknowledgements

H.Y. and H.Z. contributed equally to this work. All authors provided active and valuable feedback on the manuscript. F.X., Y.H., and H.Z. initiated the concept and designed the studies; F.X. supervised the work; H.Z. and H.Y. led the experiments and collected the overall data; H.L. designed and prepared the PDMS with bubbles. Z.M. and S.Z. contributed to the preparation of the SCL. J.L. contributed to the preparation of the PDMS with bubbles. Z.H. and S.Y. advised on the manuscript. F.X., H.Y., and Z.H. co-wrote the paper. This research was funded by National Natural Science Foundation of China (61925502). The authors are very grateful to Dr. Q.C., Nanjing Drum Tower Hospital, Affiliated Hospital of Medical School, Nanjing University, for providing us with human corneal epithelial cell lines (HCE-T). We are also very grateful to Professor D.J. and Researcher R.P. of the School of Chemistry and Chemical Engineering, Nanjing University, for their guidance and comments on the cytotoxicity testing protocol. Special thanks to Dr. Y.M. for carefully and meticulously conducting the cytotoxicity test for this work.

Conflict of Interest

The authors declare no conflict of interest.

Data Availability Statement

The data that support the findings of this study are available from the corresponding author upon reasonable request.

Keywords

environmental stability, intraocular pressure monitoring, shielding layer, smart contact lens

Received: January 13, 2024
Revised: March 27, 2024
Published online: April 9, 2024

[1] a) H. A. Quigley, *Eye.* **2018**, *33*, 254; b) S. R. Flaxman, R. R. A. Bourne, S. Resnikoff, P. Ackland, T. Braithwaite, M. V. Cicinelli, A. Das, J. B. Jonas, J. Keeffe, J. H. Kempen, J. Leasher, H. Limburg, K. Naidoo, K. Pesudovs, A. Silvester, G. A. Stevens, N. Tahhan, T. Y. Wong, H. R. Taylor, R. Bourne, P. Ackland, A. Arditi, Y. Barkana, B. Bozkurt, T. Braithwaite, A. Bron, D. Budenz, F. Cai, R. Casson, U. Chakravarthy, et al., *Lancet Global Health.* **2017**, *5*, e1221.
[2] R. N. Weinreb, P. T. Khaw, *Lancet.* **2004**, *363*, 1711.
[3] D. Peters, B. Bengtsson, A. Heijl, *Acta Ophthalmologica.* **2013**, *92*, 421.
[4] R. A. Moses, *Am. J. Ophthalmol.* **1958**, *46*, 865.
[5] a) F. Aptel, C. Musson, T. Zhou, A. Lesoin, C. Chiquet, *J. Glaucoma.* **2017**, *26*, 272; b) K. Mansouri, R. N. Weinreb, *Expert Rev. Med. Devices.* **2014**, *9*, 225.
[6] a) Y. Zhu, S. Li, J. Li, N. Falcone, Q. Cui, S. Shah, M. C. Hartel, N. Yu, P. Young, N. R. de Barros, Z. Wu, R. Haghniaz, M. Ermis, C. Wang, H. Kang, J. Lee, S. Karamikamkar, S. Ahadian, V. Jucaud, M. R. Dokmeci, H. J. Kim, A. Khademhosseini, *Adv. Mater.* **2022**, *34*, 2110389; b) H. Seo, W. G. Chung, Y. W. Kwon, S. Kim, Y.-M. Hong, W. Park, E. Kim, J. Lee, S. Lee, M. Kim, K. Lim, I. Jeong, H. Song, J.-U. Park, *Chem. Rev.* **2023**, *123*, 11488.
[7] a) H. Zhu, H. Yang, L. Zhan, Y. Chen, J. Wang, F. Xu, *ACS Sens.* **2022**, *7*, 3014; b) J. Kim, J. Park, Y.-G. Park, E. Cha, M. Ku, H. S. An, K.-P. Lee, M.-I. Huh, J. Kim, T.-S. Kim, D. W. Kim, H. K. Kim, J.-U. Park, *Nat. Biomed. Eng.* **2021**, *5*, 772; c) M. Elsherif, F. Alam, A. E. Salih, B. AlQattan, A. K. Yetisen, H. Butt, *Small.* **2021**, *17*, 2102876; d) H. Song, H. Shin, H. Seo, W. Park, B. J. Joo, J. Kim, J. Kim, H. K. Kim, J. Kim, J. U. Park, *Adv. Sci.* **2022**, *9*, 2203597; e) V. Narasimhan, R. H. Siddique, U. J. Kim, S. Lee, H. Kim, Y. Roh, Y. M. Wang, H. Choo, *Adv. Sci.* **2022**, *10*, 2205113; f) Z. Li, J. Yun, X. Li, M. Kim, J. Li, D. Lee, A. Wu, S. W. Lee, *Adv. Funct. Mater.* **2023**, *33*, 2304647; g) A. K. Yetisen, N. Jiang, C. M. Castaneda Gonzalez, Z. I. Erenoglu, J. Dong, X. Dong, S. Stößer, M. Brischwein, H. Butt, M. F. Cordeiro, M. Jakobi, O. Hayden, A. W. Koch, *Adv. Mater.* **2019**, *32*, 1902762; h) S. K. Kim, G. H. Lee, C. Jeon, H. H. Han, S. J. Kim, J. W. Mok, C. K. Joo, S. Shin, J. Y. Sim, D. Myung, Z. Bao, S. K. Hahn, *Adv. Mater.* **2022**, *34*, 2110536.
[8] a) H. An, L. Chen, X. Liu, X. Wang, Y. Liu, Z. Wu, B. Zhao, H. Zhang, *J. Micromech. Microeng.* **2021**, *31*, 035006; b) C. Yang, Q. Wu, J. Liu, J. Mo, X. Li, C. Yang, Z. Liu, J. Yang, L. Jiang, W. Chen, H.-j. Chen, J. Wang, X. Xie, *Nat. Commun.* **2022**, *13*, 2556; c) J. Kim, J. Kim, M. Ku, E. Cha, S. Ju, W. Y. Park, K. H. Kim, D. W. Kim, P.-O. Berggren, J.-U. Park, *Nano Lett.* **2019**, *20*, 1517; d) J. Zhang, K. Kim, H. J. Kim, D. Meyer, W. Park, S. A. Lee, Y. Dai, B. Kim, H. Moon, J. V. Shah, K. E. Harris, B. Collar, K. Liu, P. Irazoqui, H. Lee, S. A. Park, P. S. Kollbaum, B. W. Boudouris, C. H. Lee, *Nat. Commun.* **2022**, *13*, 5518.
[9] a) P. C. Hui, K. Shtyrkova, C. Zhou, X. Chen, J. Chodosh, C. H. Dohlman, E. I. Paschalis, *J. Biophotonics.* **2020**, *13*, 202000031; b) B. AlQattan, A. K. Yetisen, H. Butt, *ACS Nano.* **2018**, *12*, 5130; c) Z. Liu, G. Wang, C. Ye, H. Sun, W. Pei, C. Wei, W. Dai, Z. Dou, Q. Sun, C. T. Lin, Y. Wang, H. Chen, G. Shen, *Adv. Funct. Mater.* **2021**, *31*, 2010991.
[10] X. Ren, Y. Zhou, F. Lu, L. Zhai, H. Wu, Z. Chen, C. Wang, X. Zhu, Y. Xie, P. Cai, J. Xu, X. Tang, J. Li, J. Yao, Q. Jiang, B. Hu, *ACS Sens.* **2023**, *8*, 2691.
[11] A. Prashar, *Shed Tears for Diagnostics*, Springer, New York **2019**.
[12] I. K. Karunaratne, C. H. C. Lee, P. W. Or, Y. Wei, I. T. Chong, Y. Yang, M. Yu, D. C. C. Lam, *Sen. Actuators A: Phys.* **2021**, *321*,112580.
[13] G.-Z. Chen, I.-S. Chan, L. K. K. Leung, D. C. C. Lam, *Med. Eng. Phys.* **2014**, *36*, 1134.
[14] C. H. C. Lee, I. K. Karunaratne, Y. Wei, Z. Chen, I. T. Chong, Y. Yang, M. Yu, D. C. C. Lam, *Sens. Actuators, A.* **2021**, *332*,113192.
[15] A. Hajiaghajani, A. H. Afandizadeh Zargari, M. Dautta, A. Jimenez, F. Kurdahi, P. Tseng, *Nat. Electron.* **2021**, *4*, 808.
[16] a) X. Tan, J. Zheng, *Polymers.* **2022**, *14*, 1495; b) S. Masihi, M. Panahi, D. Maddipatla, A. J. Hanson, A. K. Bose, S. Hajian, V. Palaniappan,

B. B. Narakathu, B. J. Bazuin, M. Z. Atashbar, *ACS Sens.* **2021**, *6*, 938; c) Y. Kim, S. Jang, J. H. Oh, *Microelectron. Eng.* **2019**, *215*, 111002; d) J. Hwang, Y. Kim, H. Yang, J. H. Oh, *Composites, Part B.* **2021**, *211*, 108607; e) C.-R. Yang, L.-J. Wang, S.-F. Tseng, *Ceram. Int.* **2022**, *48*, 13144.

[17] M. Ku, J. Kim, J.-E. Won, W. Kang, Y.-G. Park, J. Park, J.-H. Lee, J. Cheon, H. H. Lee, J.-U. Park, *Sci. Adv.* **2020**, *6*, eabb2891.

[18] Institute of Electrical and Electronic Engineers, IEEE Standard for Safety Levels with Respect to Human Exposure to Electric, Magnetic, and Electromagnetic Fields, 0 Hz to 300 GHz, IEEE Std C95.1-2019 **2019**, https://doi.org/10.1109/IEEESTD.2019.8859679.

[19] S. R. A. Ruth, V. R. Feig, H. Tran, Z. Bao, *Adv. Funct. Mater.* **2020**, *30*, 20110991.

[20] a) Y. Zhang, T. Zhang, Z. Huang, J. Yang, *Adv. Sci.* **2022**, *9*, 2105084; b) M. Chen, L. Zhang, S. Duan, S. Jing, H. Jiang, C. Li, *Adv. Funct. Mater.* **2014**, *24*, 7548; c) S. Kang, J. Lee, S. Lee, S. Kim, J. K. Kim, H. Algadi, S. Al-Sayari, D. E. Kim, D. Kim, T. Lee, *Adv. Electron. Mater.* **2016**, *2*, 1600356.

[21] a) H. Zhou, W. Huang, Z. Xiao, S. Zhang, W. Li, J. Hu, T. Feng, J. Wu, P. Zhu, Y. Mao, *Adv. Funct. Mater.* **2022**, *32*, 2208271; b) Y. Qin, H. Xu, S. Li, D. Xu, W. Zheng, W. Wang, L. Gao, *IEEE Sens. J.* **2022**, *22*, 10446; c) H. L. Wang, T. Chen, B. Zhang, G. Wang, X. Yang, K. Wu, Y. Wang, *Small.* **2023**, *19*, 2206830.

[22] C. P. Yue, S. S. Wong, *IEEE J. Solid-State Circuits.* **1998**, *33*, 5.

[23] H. Murase, A. Sawada, K. Mochizuki, T. Yamamoto, *Jpn. J. Ophthalmol.* **2009**, *53*, 1.

[24] Canino3d, Free Cartoon Game Man Character (Rigged), https://skfb.ly/oSB7p, (accessed: March 2024).

[25] S. Assawaworrarit, X. Yu, S. Fan, *Nature.* **2017**, *546*, 387.